Evolution of Fe redox state in serpentine during subduction

Baptiste Debret [a,b,c,*], Muriel Andreani [d], Manuel Muñoz [e], Nathalie Bolfan-Casanova [a,b,c], Julie Carlut [f], Christian Nicollet [a,b,c], Stéphane Schwartz [e], Nicolas Trcera [g]

[a] Clermont Université, Université Blaise Pascal, Laboratoire Magmas et Volcans, Clermont-Ferrand, France
[b] CNRS, UMR6524, LMV, Clermont-Ferrand, France
[c] IRD, R163, LMV, Clermont-Ferrand, France
[d] Laboratoire de Géologie de Lyon, UMR5276, ENS – Université Lyon 1, Villeurbanne, France
[e] Institut des Sciences de la Terre, Université Grenoble I, Grenoble, France
[f] Institut de Physique du Globe de Paris, France
[g] Synchrotron SOLEIL, Paris, France

ARTICLE INFO

ABSTRACT

Serpentinites are an important component of the oceanic lithosphere that formed at slow to ultra-slow spreading centers. Serpentine could thus be one of the most abundant hydrous minerals recycled into the mantle in subduction zones. Prograde metamorphism in subducted serpentinites is characterized by the destabilization of lizardite into antigorite, and then into secondary olivine. The nature of the fluid released during these phase transitions is controlled by redox reactions and can be inferred from oxidation state of Fe in serpentine minerals. We used bulk rock analyses, magnetic measurements, SEM observations and μXANES spectroscopy to establish the evolution of $Fe_2O_3{}^{Tot}{}_{(BR)}$ and magnetite content in serpentinite and Fe oxidation state in serpentine minerals from ridge to subduction settings.

At mid-ocean ridges, during the alteration of peridotite into serpentinite, iron is mainly redistributed between magnetite and oceanic serpentine (usually lizardite). The Fe^{3+}/Fe_{Total} ratio in lizardite and the modal percentage of magnetite progressively increase with the degree of local serpentinization to maxima of about 0.8 and 7 wt%, respectively, in fully serpentinized peridotites. During subduction, the $Fe_2O_3{}^{Tot}{}_{(BR)}$ of serpentinite remains constant (∼7–10 wt%, depending on the initial Fe content of the peridotite) while the modal percentage of magnetite decreases to less than 2% in eclogite facies rocks. The Fe^{3+}/Fe_{Total} ratio in serpentine also decreases down to 0.2–0.4 in antigorite at eclogite facies.

Our results show that, in the first 70 km of subduction, the transition from lizardite to antigorite is accompanied by a reduction of Fe in bulk rock samples and in serpentine minerals. This redox reaction might be coupled with the oxidation of reduced oceanic phases such as sulfides, and the formation of oxidized fluids (e.g. SO_X, H_2O, CO_X). At greater depths, the beginning of antigorite dehydration leads to an increase of Fe^{3+}/Fe_{Total} in relict antigorite, in agreement with the preferential partitioning of ferric iron into serpentine rather than into olivine.

1. Introduction

Fluids released during subduction of the oceanic lithosphere are the primary cause of melting in the mantle wedge and arc magmatism. Those magmas commonly display higher Fe^{3+}/Fe_{Total} ratios relative to those of mid-ocean ridge and ocean-island basalts (MORB and OIB, respectively) suggesting that the fluids released from the slab upon subduction are oxidized, i.e. dominated by H_2O, CO_2 and SO_X species (Arculus, 1994; Evans and Tomkins, 2011; Kelley and Cottrell, 2009; Stolper and Newman, 1994). Those conclusions are consistent with geochemical studies of mantle wedge xenoliths (Andersen and Neumann, 2001; Parkinson and Arculus, 1999). However, recent results based on V/Sc ratios (Lee et al., 2010), fluid inclusions (Song et al., 2009) and thermochemical modeling (Malvoisin et al., 2011) have suggested that reduced fluids are present in subduction zone. These discrepancies emphasize the difficulty in assessing the nature of slab-derived fluids and their respective oxidation states.

The oxidation state of the rocks forming the lithosphere controls the speciation of C-S-O-H-bearing fluids (Frost and McCammon, 2008) that play a fundamental role in metasomatic processes

in subduction zones. As hydrous minerals are intimately linked to subduction processes, the nature of the released fluids is controlled by redox reactions during hydrous mineral phase change or dehydration. Serpentinites form through the hydration of oceanic lithosphere at slow spreading centers (Mével, 2003) and are an important component of subduction zones (Hattori and Guillot, 2007; Reynard, 2013). Furthermore, since they contain up to ∼12 wt% of water, they constitute a large reservoir of water compared to other hydrous rocks forming the oceanic lithosphere and may therefore play a major role in the transfer of fluids in subduction zones.

At slow or ultra-slow spreading ridges, the upper 3–6 km of oceanic lithosphere are highly serpentinized (Cannat et al., 2000, 1995, 2010). The serpentinization of ultra-mafic rocks is associated with magnetite formation (Bach et al., 2006; Oufi et al., 2002), while the fluids discharged from serpentinites can be H_2 and CH_4 rich (Charlou et al., 2002; Marcaillou et al., 2011). These observations indicate that olivine-hosted Fe becomes oxidized as water is reduced during serpentine crystallization (Berndt et al., 1996; Klein and Bach, 2009; Klein et al., 2009; McCollom and Bach, 2009; Seyfried et al., 2007). Recent studies have shown that the increase of the serpentinization degree of the peridotite is correlated with an increase of the magnetite mode and Fe^{3+}/Fe_{Total} ratio of the serpentine (Andreani et al., 2013; Marcaillou et al., 2011). These observations imply that the serpentinites that constitute the upper oceanic lithosphere and which are ultimately subducted are highly oxidized relative to mantle peridotites.

During subduction, serpentinites are situated in the upper 3–6 km of the slab (Debret et al., 2013a; Reynard et al., 2010). With prograde metamorphism, the progressive serpentine phase changes (lizardite → antigorite → olivine/pyroxene) drive fluid release to the mantle wedge (Hattori and Guillot, 2007) until depths of about 150–180 km, where dehydration of serpentine to form olivine, enstatite and chlorite assemblages (Trommsdorff et al., 1998; Fumagalli and Poli, 2005) should be complete (Ulmer and Trommsdorff, 1995; Wunder and Schreyer, 1997). Geochemical observations based on fluid mobile element (B, Li, As, Sb, Ba, Rb and Cs), halogens (F, Cl) and volatiles (S) behavior during prograde metamorphism in subduction zones reveal a direct link between the composition of the fluid released during serpentine phase transitions and those of arc magmas (Debret et al., 2013b, 2014; Savov et al., 2005, 2007; Scambelluri and Tonarini, 2012; Vils et al., 2011). Nonetheless, there is no overall consensus on the evolution of the redox state of serpentinites during subduction.

Exhumed high-pressure serpentinites in ophiolites from localities such as the Western Alps provide an alternative means of constraining the redox state of slab-derived fluids. Indeed, these ophiolites are considered to have been highly hydrated and serpentinized during an oceanic stage (distal continental margin or mid-ocean ridge environment) prior to partial dehydration during prograde metamorphism (Debret et al., 2013a, 2013b; Hattori and Guillot, 2007; Lafay et al., 2013; Li et al., 2004; Schwartz et al., 2013; Vils et al., 2011). Here we propose to use the redox state of iron in serpentinites, an abundant element in this type of rock, in order to assess the possible nature of the released fluids during serpentine phase changes in subduction zones. We provide the first in-situ (μXANES spectroscopy) and bulk rock chemistry measurements of Fe redox state from alpine serpentinites, which record different P–T conditions representative of a cross section trough a subducting slab. In contrast to arc magmas, which may have undergone processes such as crystal fractionation or assimilation, these samples provide a relatively direct means of constraining the redox state of subducted lithosphere. Furthermore, the study of high-pressure metamorphic rocks allows changes in Fe redox state as a function of serpentine metamorphism during subduction to be directly constrained.
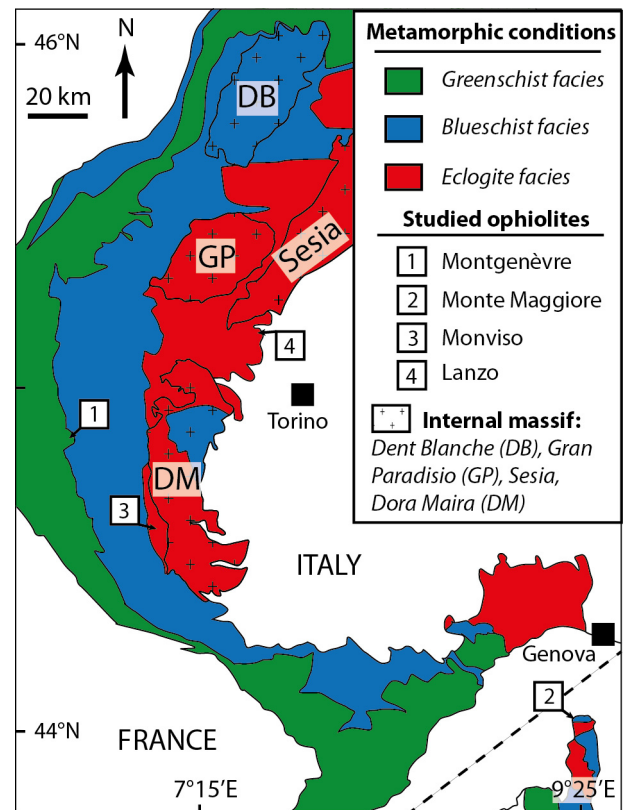

Fig. 1. Geological map of the Western Alps showing the metamorphic facies and the spatial distribution of studied ophiolites. The numbers indicate the studied ophiolites: 1. The Mont Genèvre ophiolites (Chenaillet and Punta Rascia massifs); 2. Monte Maggiore ophiolite; 3. Mon Viso ophiolite and 4/Lanzo ophiolite.

2. Geological setting and petrographic observations

The Western Alps formed as the result of the subduction of the Tethyan oceanic lithosphere beneath Apulia between late Jurassic and early Tertiary (Lombardo et al., 2002). The Tethyan oceanic lithosphere is an equivalent to the modern Atlantic Ocean lithosphere (Lagabrielle and Cannat, 1990) and is composed of intrusive gabbroic pods surrounded by serpentinites and sometimes topped by basalts and/or sediments (Cannat et al., 1995). In order to study the redox state of Fe along prograde metamorphism, we sampled various alpine meta-ophiolites recording different metamorphic conditions (Fig. 1) representative of a subduction gradient. Two main phase transitions are observed in the serpentinites of this metamorphic suite: the transition from lizardite to antigorite that occurs from greenschist to blueschist facies at ∼300–400 °C (Evans, 2004; Schwartz et al., 2013), and the dehydration of antigorite into secondary olivine at T > 600 °C in the eclogitic facies (Bromiley and Pawley, 2003).

Oceanic serpentinites have been widely described and are known to be mostly composed of lizardite, the low-pressure/low-temperature (LP/LT) variety of serpentine (Evans, 2004), and of chrysotile (Andreani et al., 2007; Mével, 2003). They form pseudomorphic mesh and bastite textures, replacing olivine and orthopyroxene respectively (Mével, 2003). The mesh texture appears grey under cross polarized light and forms homogenous areas of lizardite with finely disseminated magnetite. The mesh cell is delimited by fibrous lizardite rims associated with stringy magnetite aggregates (Fig. 2a). The magnetite strings consist of euhedral magnetite grains in equilibrium with the surrounding lizardite (Fig. 2b). Bastite textures consist of white serpentine grains elongated parallel to the original orthopyroxene cleavages (Fig. 2a) while clinopyroxene is typically resistant to low temper-
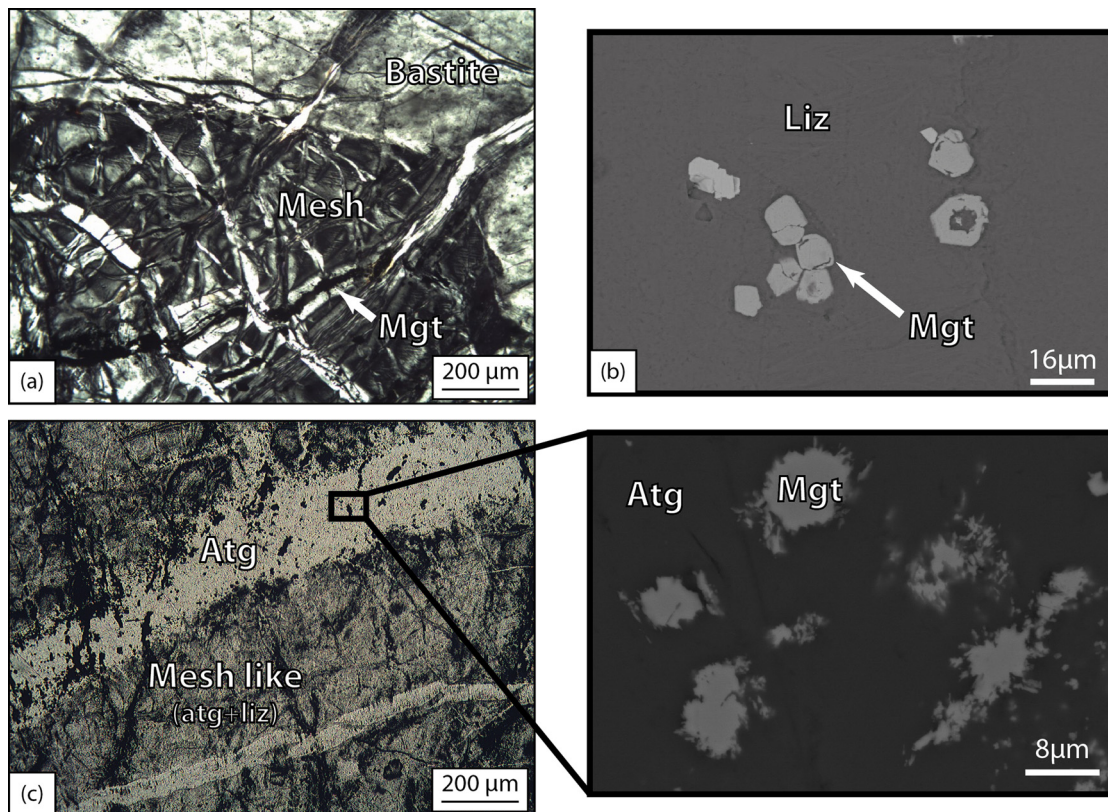
Fig. 2. (a) Photomicrograph in crossed polarized light showing typical mesh and bastite textures. The mesh rims are associated with a fine string of magnetite. (b) SEM photomicrograph in back scattered electron (BSE) of magnetite grains associated with mesh texture. (c) Photomicrograph in plane polarized light (left photo) and BSE (right photo) of a serpentinite from the Montgenèvre ophiolite. The mesh like texture is composed of lizardite (Liz) and antigorite (Atg) intergrown on a micrometer scale. A late antigorite vein crosses the mesh texture. The magnetite grains associated with both textures display indented boundaries (right photo).

ature serpentinization (Andreani et al., 2007; Klein et al., 2013; Mével, 2003).

2.1. The Montgenèvre ophiolite

The Montgenèvre ophiolite is located in the external Piemont zone, 6 km west of Briançon (Fig. 1). It is a thin klippe resting onto the Lago Nero Unit (Caby, 1995). The massif is composed of metagabbro pods occasionally topped by basalts that display greenschist parageneses (Mével et al., 1978), and are surrounded by massive serpentinites (serpentinization >80%). The massif is commonly interpreted as an oceanic portion of the upper part of the Tethyan oceanic lithosphere (Chalot-Prat, 2005; Manatschal et al., 2011). Most of serpentinites are composed of lizardite and chrysotile assemblages displaying mesh and bastite textures (Liz-serpentinites) crystallized in an oceanic setting (Schwartz et al., 2013; Lafay et al., 2013). The local crystallization of antigorite, high-pressure and high-temperature serpentine variety (HP/HT) (Wunder et al., 2001), at the expense of lizardite (Atg/Liz-serpentinites) can be interpreted in terms of an increase in P–T conditions during subduction. It is marked in thin section by the partial recrystallization of mesh and bastite textures into antigorite, which display intermediate Raman spectra between lizardite and antigorite (mesh-like and bastite-like textures; see Debret et al., 2013a for further details), and by the occurrence of pure antigorite veins crossing oceanic textures (Fig. 2c). The magnetite grains observed in antigorite veins and within mesh-like rims display indented boundaries interpreted as dissolution textures (Fig. 2c). In contact with pure antigorite, the primary spinel is zoned: it has an Al–Cr–Fe core surrounded by a thin double corona (<30 μm) of chromite and magnetite.

2.2. The Monte Maggiore ophiolite

The Monte Maggiore ophiolite is located in the northern end of the Cap Corse, Northern Corsica (Fig. 1). It is an ultramafic body of ~4 km^2 surrounded by eclogitized continental units. The massif is a fragment of oceanic lithosphere generated in an ocean–continent transition (OCT) context (Jackson and Ohnenstetter, 1981; Piccardo and Guarnieri, 2010). It is composed of slightly serpentinized peridotites (SSP; <20% serpentinization) intruded by mafic pods and dykes displaying blueschist facies paragenesis (Nicollet et al., 2001; Vitale Brovarone et al., 2013). The SSP are plagioclase- and/or spinel-harzburgites and lherzolites. They are affected by two main serpentinization episodes (Debret et al., 2014): the first one corresponds to the crystallization of lizardite veins from primary minerals during massif oceanization and the second event corresponds to antigorite veins formed from lizardite and primary minerals during subduction prograde HP metamorphism. In the southern part, the massif is bordered by a serpentinite envelope of <1 km-wide. This envelope is affected by an East–West foliation that surrounds boudins of massive serpentinite. The foliated serpentinites are mostly composed of antigorite (Atg-serpentinites) while the massive boudins are composed of mesh- and bastite-like textures and pure antigorite (Atg/Liz-serpentinites). At mesh-like rims, the lizardite and magnetite are replaced by thin lamellae of antigorite with only rare relicts of magnetite displaying indented boundaries (Fig. 3a). In these rocks, the primary spinel is coronitic: at the contact of antigorite, it is recrystallized into a chromite–magnetite (Mgt2) assemblage (Fig. 3b). The clinopyroxene has a coronitic texture composed of antigorite lamellae associated with magnetite grains (Fig. 3c). The magnetite grains are sub-euhedral attesting that they are equilibrated with the surrounding antigorite (Fig. 3c): they constitute a new generation of magnetite (Mgt2).
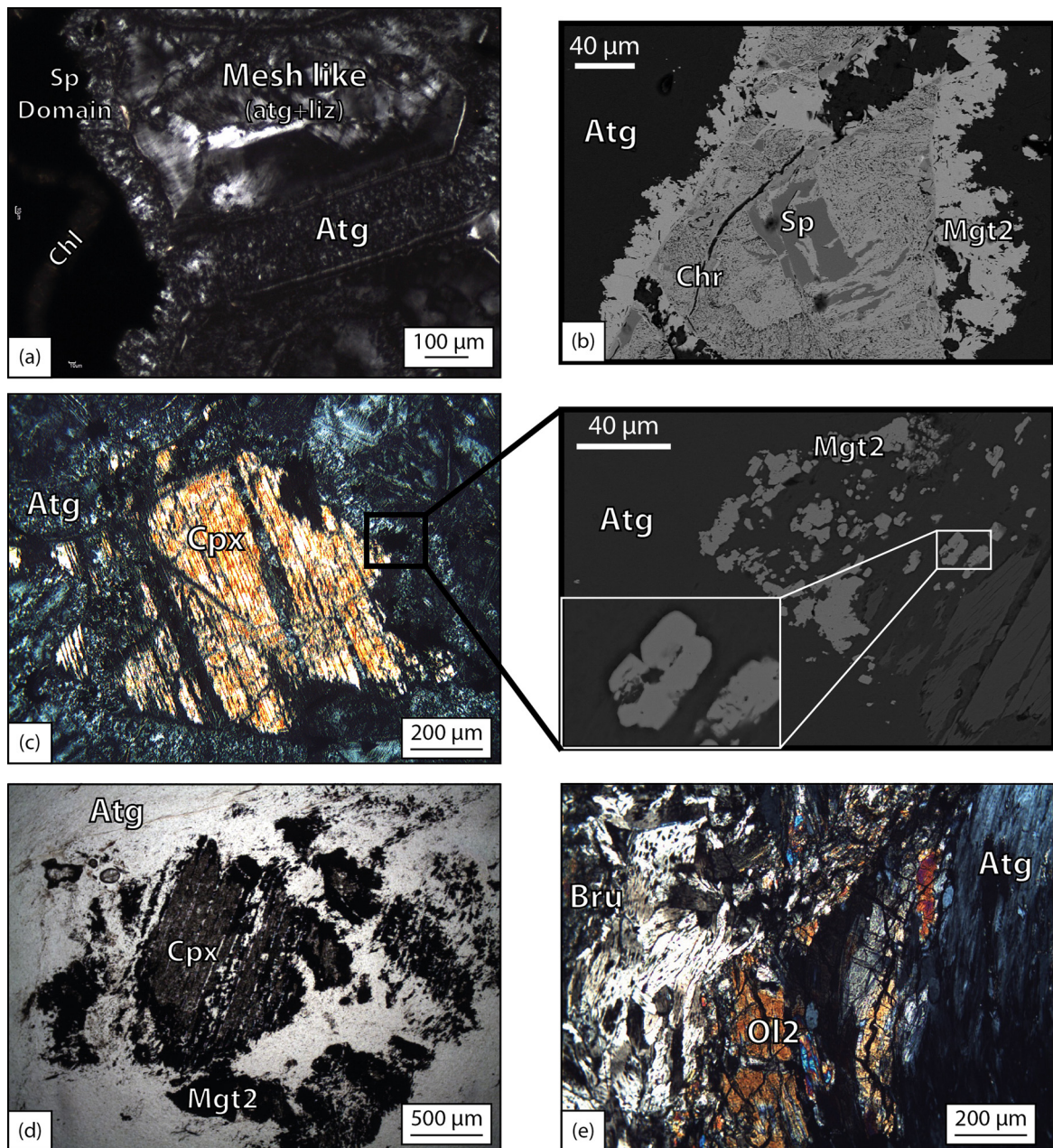
Fig. 3. (a) Photomicrograph in crossed polarized light of serpentinite from Monte Maggiore. Mesh rims are recrystallized into thin lamellae of antigorite. The mesh core is composed of lizardite and antigorite associated at nano-scale (Mesh-like texture). (b) SEM microphotography in BSE of a spinel domain from Monte Maggiore serpentinite. In contact with antigorite, the primary spinel (Sp) displays a double corona composed of chromite (Chr) and magnetite (Mgt2). (c) Photomicrograph in crossed polarized light (left photo) and in BSE (right photo) of a serpentinite from Monte Maggiore. The clinopyroxene relict is surrounded by an antigorite and magnetite corona. The magnetite associated with the antigorite corona is sub-euhedral (Mgt2, right photos). (d) Photomicrograph in plane polarized light of a clinopyroxene relict partly recrystallized into antigorite and secondary magnetite. In the left corners of the photo, the olivine domain is composed of antigorite without magnetite. (e) Photomicrograph in crossed polarized light of secondary olivine (Ol2) formed at the expense of brucite (Bru) and antigorite from a Monviso serpentinite.

2.3. The Monviso massif

The Monviso massif is buried between the Dora Maira massif and the Queyras accretionary prism (Fig. 1). It represents oceanic lithosphere fragments blended during massif exhumation (Schwartz et al., 2001). It is composed of metagabbroic pods metamorphosed under the eclogite facies and massive serpentinites boudins surrounded by foliated serpentinites (Schwartz et al., 2001). Massive serpentinites are mostly composed of antigorite (Atg-serpentinites). Few relicts of mesh-like textures are observed in these rocks and can be interpreted as relicts of oceanic serpen-

tinization. The foliated serpentinites are greatly recrystallized into antigorite lamellae (Fig. 3d): the olivine domain is replaced by thin antigorite lamellae of <5 μm and the orthopyroxene domain by antigorite lamellae of ∼20–50 μm long. The spinel domain is composed of chromite and magnetite assemblages of ∼100 μm width. Clinopyroxene has recrystallized into oriented antigorite lamellae of ∼20–50 μm long associated with secondary magnetite aggregates; the primary clinopyroxene is sometimes preserved in the center of these aggregates (Fig. 3d). Locally, prograde antigorite is partly dehydrated into secondary olivine at eclogite facies conditions (Schwartz et al., 2013).

2.4. The Lanzo massif

The Lanzo massif is an eclogitized ultramafic body of 150 km^2 bounded by the sediments of the Po plain to the East and South, by meta-ophiolites and the Schistes Lustrés unit in the West, and by the HP metamorphic continental unit of Sesia in the North (Pelletier and Müntener, 2006). The massif is a portion of oceanic lithosphere preserving its oceanic structure (Debret et al., 2013a; Lagabrielle et al., 1989). It is composed of a central part of SSP surrounded by a serpentinite envelope of 3–5 km width. The ultramafic rocks record different steps of serpentinization (Debret et al., 2013a): lizardite crystallization during an oceanic serpentinization step; prograde and retrograde antigorite crystallization during subduction and massif exhumation; locally secondary olivine granoblasts of ∼20 μm formed at the expense of prograde antigorite and magnetite at metamorphism peak condition of the massif. As observed in the Monviso serpentinites, in the serpentinite envelope, the olivine domain is replaced by thin antigorite lamellae thinner than 5 μm, the spinel domain by chromite and magnetite assemblages of ∼100 μm widths, and the pyroxene domain by antigorite lamellae of ∼20–50 μm sometimes associated with magnetite masses of ∼20 μm widths.

A set of 13 serpentinites and 6 SSP representatives of serpentine phase changes during prograde metamorphism were selected for this study (Table 1). Most of these samples have already been characterized in previous petrological (Debret et al., 2013a; Schwartz et al., 2013) and geochemical (Debret et al., 2013b; Lafay et al., 2013) studies. The metamorphic conditions and petrographic characteristics of the studied samples are summarized in Table 1. In the Liz/Atg- and Atg-serpentinites no retrograde phases (e.g. talc, chrysotile amphiboles; Padrón-Navarta et al., 2011; Müntener et al., 2000) are observed suggesting that they were little affected by retrograde metamorphism. In the Liz/Atg-serpentinites, antigorite is observed to have formed at the expense of mesh and bastite textures (Figs. 2c and 3a). We therefore assume that antigorite crystallization is relative to prograde metamorphism stage.

3. Methods

3.1. Bulk rock analyses

Bulk rock powders for major elements measurements were prepared with the addition of Li-metaborate. The melts obtained by fusion of this mixture in a magnetic induction oven were subsequently quenched and diluted by a factor of 2000 for analysis. Major element concentrations were determined by ICP-AES at the Laboratoire Magmas et Volcans of Clermont-Ferrand (France). Concentrations were calibrated against the DRN basaltic glass. Precision on samples were determined by repeated analyses of the reference basalt BHVO. This typically resulted in a better than 1% precision for all measured elements. Additional Fe^{2+} analyses of bulk rock (BR) samples were performed at the SARM-CRPG (Nancy, France). These analyses were done by automatic titration at the equivalent point with potassium dichromate after dissolution of the sample in a HF/H_2SO_4 mixture, in the presence of H_3BO_3 and H_3PO_4. Subsequently $Fe^{3+}/Fe_{Total\,(BR)}$ ratios were calculated from the measuring $Fe_2O_3^{Tot}{}_{(BR)}$ and $Fe^{2+Tot}{}_{(BR)}$ values (e.g. Andreani et al., 2013).

3.2. Hysteresis measurements

The amount of magnetite in serpentinite samples can be estimated from the saturation magnetization derived from hysteresis magnetic measurements. Hysteresis cycles at room temperature up to maximum field of 500 mT to 700 mT were measured using a Princeton Vibrating Sample Magnetometer (VSM) at IPGP Paris. At least two fragments of ∼1 cm^3 for each serpentinite samples were used and the saturation magnetization was then determined by taking the average value. The saturation magnetization of the serpentinite depends linearly on concentration of magnetite; this calculation is made using a proportionality factor of 92 A m^2/kg between Js and the nominal weight of magnetite (Malvoisin et al., 2012; O'Reilly, 1984).

3.3. In-situ analyses

In situ major element analyses of minerals of ultramafic rocks were performed with a microprobe CAMECA SX 100 at the Laboratoire Magmas et Volcans in Clermont Ferrand (France). Microprobe analysis mean values and FeO maximal and minimal values of repeated analysis of serpentine and secondary olivine forming serpentinites and SSP are given in Appendix A, MMC 1.

Iron speciation was measured by X-ray absorption spectroscopy at the iron K-edge at the LUCIA beamline of SOLEIL synchrotron (Source Optimisée de Lumière d'Energie Intermédiaire du LURE, France). Measurements were operated with a current and energy of 400 mA and 2.75 GeV, respectively. The X-ray absorption near edge structure (XANES) spectra were collected using a Si(311) double crystal monochromator. The energy calibration was performed using an iron foil. XANES spectra were measured in fluorescence mode using a four-element silicon drift diode (SDD) detector with a total active area of 40 mm^2. The beam spot size was set to 4 × 4 μm^2 by using two dynamically bendable mirrors in Kirkpatrick–Baez configuration.

XANES spectra were acquired from 7050 eV to 7300 eV with a sampling step of 0.1 eV in the pre-edge region. In order to minimize potential photo-oxidation effects (Appendix A, MMC 2), the dwell time was adjusted to 0.5 s per point, resulting in a total acquisition time of 12 min. To improve signal-to-noise ratio, each XANES spectrum is the average of 4 spectra acquired on 4 distinct locations, separated by 30 μm, in a same serpentine texture. X-ray fluorescence (XRF) chemical maps were used to identify minerals in the thin sections and to selected spots for XANES measurements.

XANES spectra were normalized using the Athena© software (Ravel and Newville, 2005). Following previous XANES studies (e.g. Berry et al., 2003, 2010; Bolfan et al., 2012; Farges et al., 2001; Muñoz et al., 2013; Wilke et al., 2001), the Fe^{3+}/Fe_{Total} ratio of serpentines were derived by fitting the pre-edge region (shown in Fig. 4) using PeakFit© software. The background of the pre-edge region was modeled using the tail of a Gaussian function and the pre-edge peak was deconvoluted using two pseudo-Voigt functions. This treatment results in absolute uncertainties for the determination of the pre-edge centroid of ±0.05 eV in energy, and ±0.025 in integrated area (e.g. Muñoz et al., 2013; Wilke et al., 2001). The Fe^{3+}/Fe_{Total} was derived directly from the variogram of Wilke et al. (2001). This variogram was reproduced by measuring three powdered standard compounds namely olivine ($^{VI}Fe^{2+}$), andradite ($^{VI}Fe^{3+}$) and sanidine ($^{IV}Fe^{3+}$), previously characterized in other studies (Andreani et al., 2013; Marcaillou et al., 2011; Muñoz et al., 2013).

Previous studies reported important changes for XANES spectra and pre-edge peaks depending on crystal orientation relative to the polarized X-ray beam (Bolfan et al., 2012; Evans et al., 2014; Muñoz et al., 2013). Nevertheless, a recent comparison between the XANES spectra of antigorite crystals and powders revealed that maximal orientation effects of antigorites were reduced relative to other phyllosilicates (Muñoz et al., 2013). Due to the unknown orientation of antigorite crystals, Fe^{3+}/Fe_{Total} might be underestimated by a maximum of 0.1 or overestimated by 0.05.

Table 1

Bulk rock analysis of serpentinites and SSP. The error on major element content is smaller than 0.5 wt%.

Rock	Serpentinite													SSP			
Metamorphic facies	Greenschist				Blueschist				Eclogite					Blueschist		Eclogite	
Locality	Mont Genèvre				Monte Maggiore				Monviso	Lanzo		Lanzo	Monviso	Monte Maggiore		Lanzo	
Sample name	ICH02	Bch10	Bch6	Bch9	MM8	MM15	MM19	MM2	Vis1	LZ14b	RO1	LZ27a1	Vis5b	MAG33	MAG26	LZ17a	LZ19
Rock type	Liz-serpentinite		Atg/Liz-serpentinite		Atg/Liz-serpentinite		Atg-serp		Atg/Liz-serp.	Atg-serpentinite		Ol2/Atg-serpentinite					
Serpentine minerals	Liz	Liz	Liz ± Atg	Liz, Atg	Liz, Atg	Liz, Atg	Atg ± Liz	Atg	Liz, Atg	Atg	Atg ± Ol2	Atg, Ol2	Atg, Ol2	Liz ± Atg	Atg ± Liz	Liz, Atg	Atg, Ol2
SiO_2	39.6	38.8	39.2	40.2	38.6	39.5	39.1	40.1	40.0	39.0	39.7	40.0	38.3	41.1	42.1	42.6	41.9
Al_2O_3	1.0	2.0	2.6	3.0	1.9	2.1	2.0	1.8	2.0	2.4	2.8	2.3	1.3	2.3	2.2	2.6	3.0
Fe_2O_3	7.8	8.1	7.9	7.9	9.5	7.9	8.9	8.0	8.1	8.4	8.1	8.5	9.2	8.4	8.3	8.9	8.9
MgO	37.9	37.8	36.5	36.0	37.4	36.3	38.3	37.8	36.2	38.1	36.0	38.5	40.1	39.5	40.1	39.5	38.6
CaO	0.1	1.0	1.3	1.8	0.9	1.9	0.4	0.7	2.6	0.0	2.1	1.5	0.9	2.2	2.4	2.6	3.1
Na_2O	b.d.l.	0.0	0.0	0.0	0.0	0.0	0.0	0.0	b.d.l.	0.3	0.2	0.3	b.d.l.	0.0	0.0	0.1	0.1
K_2O	b.d.l.	0.0	0.0	b.d.l.	b.d.l.	0.0	0.0	0.0	b.d.l.	0.3	0.2	0.2	0.0	0.1	0.1	b.d.l.	b.d.l.
TiO_2	0.0	0.1	0.1	0.1	0.1	0.1	0.1	0.0	0.0	0.1	0.1	0.1	0.0	0.1	0.1	0.1	0.1
MnO	0.1	0.1	0.1	0.1	0.1	0.1	0.1	0.1	0.1	0.0	0.1	0.1	0.1	0.1	0.1	0.1	0.1
P_2O_5	b.d.l.	0.0	0.0	0.0	0.0	0.0	0.0	0.0	0.0	0.0	0.0	0.0	0.0	0.0	0.0	0.0	0.0
LOI	13.2	12.1	11.8	11.0	12.1	11.3	10.9	11.6	10.4	11.3	10.5	7.9	9.9	6.0	4.2	3.1	3.4
Tot	99.6	100.1	99.6	100.3	100.6	99.3	99.7	100.2	99.3	100.1	99.9	99.5	99.9	99.8	99.6	99.7	99.3
FeO (Fe^{2+} titration)	2.1	2.7	2.8	3.3	2.8	3.7	4.8	3.0	3.5	3.6	3.6	6.3	4.2	5.5	7.1	6.5	7.0
Fe^{3+}/Fe^{Tot}	0.7	0.6	0.6	0.6	0.7	0.5	0.4	0.6	0.5	0.5	0.5	0.2	0.5	0.3	0.1	0.2	0.2
%Mag (stdr deviation)	6(0.4)	6.1(1.5)	3.4(0.9)	3.2(1.0)	4.9(1.3)	2.2(1)	1.2(0.2)	1.4(0.5)	3.4(0.8)	1.8(0.7)	1(0.1)	<1	1.2(0.9)	<1	<1	<1	<1
Analyzed fragments	3	4	4	2	2	2	2	2	2	4	2	1	2	1	1	1	1

b.d.l.: below detection limit.

Table 2

Pre-edge characteristics of XANES standards and serpentine minerals. The XANES standards have been measured with exactly the same conditions as the sample data set and during the same run.

Sample	Mineral	Texture	Pre-edge centroid		Fe^{3+}/Fe_{Total}	Error Fe^{3+}/Fe_{Total} ($\pm$)
			Area	Position		
Standards	Olivine		0.079	7112.96	0	
	Sanidine		0.457	7114.19	1	
	Andradite		0.158	7114.19	1	
Serpentinites						
ICh02	Liz	Mesh	0.184	7114.14	0.93	0.06
BCh6	Liz $\pm$ Atg	Mesh	0.165	7114.07	0.85	0.06
	Liz, Atg	Vein	0.156	7114.17	0.97	0.06
	Liz, Atg	Vein	0.171	7114.08	0.85	0.06
	Liz, Atg	Vein	0.207	7114.08	0.84	0.06
BCh9	Liz, Atg	Mesh	0.188	7114.02	0.76	0.07
	Liz, Atg	Mesh	0.176	7114.07	0.83	0.06
	Liz, Atg	Mesh	0.199	7114.05	0.80	0.08
	Liz, Atg	Mesh	0.151	7113.97	0.74	0.06
	Atg	Vein	0.153	7113.94	0.68	0.06
	Atg	Vein	0.139	7113.92	0.69	0.05
	Atg	Vein	0.142	7113.77	0.50	0.06
MM8	Liz, Atg	Mesh	0.134	7114.14	0.93	0.06
	Liz, Atg	Mesh	0.133	7114.02	0.80	0.06
	Liz, Atg	Mesh	0.129	7114.06	0.85	0.06
	Liz, Atg	Mesh	0.126	7114.04	0.83	0.06
	Liz, Atg	Mesh	0.124	7114.02	0.80	0.06
	Liz, Atg	Mesh	0.139	7114.09	0.87	0.05
	Atg	Mesh rim	0.133	7114.03	0.81	0.05
	Atg	Mesh rim	0.125	7114.07	0.86	0.05
	Atg	Cpx rim	0.177	7114.04	0.80	0.06
	Atg	Cpx rim	0.162	7114.07	0.84	0.06
	Atg	Cpx rim	0.138	7114.08	0.87	0.06
	Atg	Sp rim	0.141	7114.15	0.95	0.06
	Atg	Sp rim	0.144	7114.06	0.84	0.06
LZ14b	Atg	–	0.120	7113.74	0.52	0.05
Vis5b	Atg	Associated with Ol2	0.114	7113.84	0.63	0.05
LZ27a1	Atg	Associated with Ol2	0.131	7113.69	0.44	0.06
SSP						
LZ17	Liz	Vein	0.123	7113.94	0.72	0.06
	Atg	Vein	0.145	7113.69	0.39	0.08
Mag32	Liz	Vein	0.134	7113.86	0.62	0.05
	Liz	Vein	0.122	7113.90	0.67	0.05
LZ35c	Atg	Vein	0.122	7113.64	0.40	0.05
	Atg	Vein	0.131	7113.50	0.13	0.10
LZ19	Atg	Vein associated with Ol2	0.123	7113.72	0.49	0.05
LZ34b	Atg	Vein associated with Ol2	0.128	7113.85	0.62	0.06
	Atg	Vein associated with Ol2	0.134	7113.78	0.53	0.05

Moreover, the same authors mention that areas of the pre-edge do not change significantly with crystal orientation.

The centroid energy and integrated area of the pre-edge peaks are displayed in Figs. 5a and 5b and are reported in Table 2; including uncertainty estimates. The entire dataset of serpentine plots in the $^{VI}Fe^{2+}$–$^{VI}Fe^{3+}$–$^{IV}Fe^{3+}$ region (Fig. 5). This suggests the absence of Fe^{2+} in serpentine tetrahedra and the occurrence of Fe^{3+} in serpentine octahedra and tetrahedra as proposed in previous crystallographic and chemical studies (Andreani et al., 2013; Fuchs et al., 1998; Marcaillou et al., 2011; O'Hanley and Dyar, 1993).

4. Results

4.1. Bulk rock analysis

Among the selected samples, there is no obvious change in $Fe_2O_3^{Tot}{}_{(BR)}$ (BR: Bulk Rock) with prograde metamorphism, indicating that Fe is immobile in serpentinites during subduction (Table 1). The $Fe_2O_3^{Tot}{}_{(BR)}$ content ranges from 7.79 to 9.53 wt%

(Table 1) and these slight variations most probably reflect variations in the modal abundances of the protolith minerals; it has previously been shown that the major element compositions of serpentines are mainly controlled by primary mineralogy (Godard et al., 2008; Mével, 2003; Paulick et al., 2006). Furthermore, according to previous geochemical studies on these samples (Debret et al., 2013b; Lafay et al., 2013), the selected serpentinites have primary mineral modes similar to plagioclase/spinel lherzolites. The different $Fe_2O_3^{Tot}{}_{(BR)}$ contents among the selected samples are thus attributed to slight variations in clinopyroxene, spinel and plagioclase contents. The $Fe_2O_3^{Tot}{}_{(BR)}$-poor serpentinites are formed from spinel- and clinopyroxene-poor lherzolites while the $Fe_2O_3^{Tot}{}_{(BR)}$-rich serpentinites are formed from spinel- and clinopyroxene-rich lherzolites.

In the serpentinites, the $Fe^{3+}/Fe_{Total\,(BR)}$ decreases with the metamorphic grade (Fig. 6a). At the Montgenèvre ophiolite, the Liz-serpentinites have a $Fe^{3+}/Fe_{Total\,(BR)}$ ratio ranging from 0.65 to 0.7 while the Atg/Liz-serpentinites display lower $Fe^{3+}/Fe_{Total\,(BR)}$ ratio ranging from 0.56 to 0.62. At the Monte Maggiore, the Atg/Liz-serpentinites have a $Fe^{3+}/Fe_{Total\,(BR)}$ ratio varying from 0.51 to 0.68
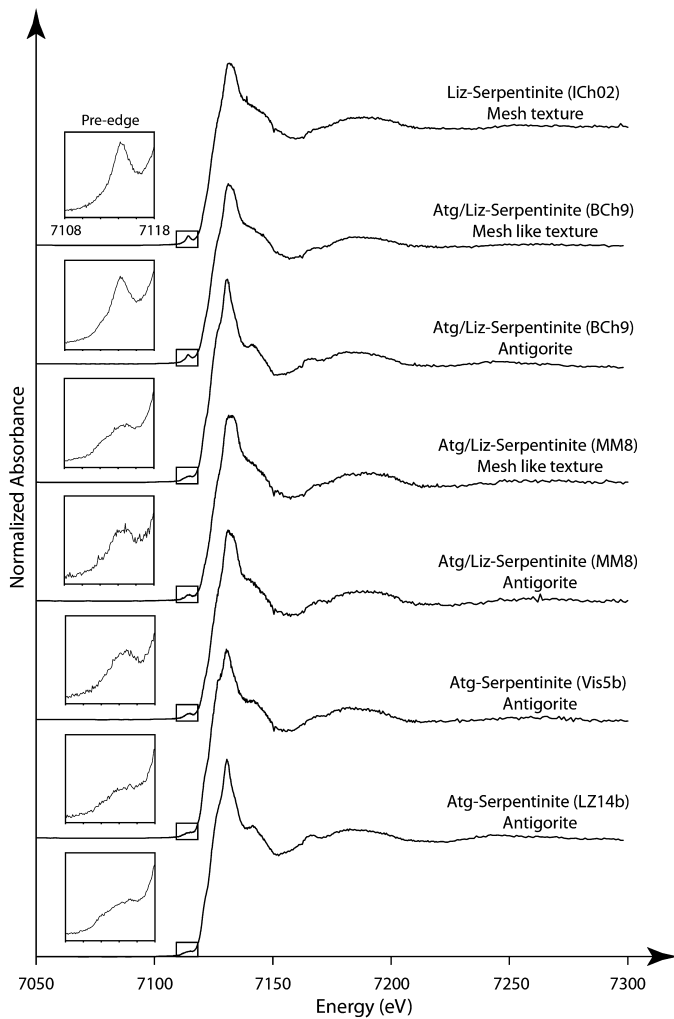
Fig. 4. Spectral signature at the K-edge for the different serpentine textures in the Montgenevre (ICh02, BCh9), Monte Maggiore (MM8), Monviso (Vis5b) and Lanzo (LZ14b) massifs. The box shows the pre-edge region of each XANES spectra.

and the one of Atg-serpentinites varies from 0.43 to 0.6. Under eclogite facies (Monviso and Lanzo massif), the $Fe^{3+}/Fe_{Total\,(BR)}$ ratio in the Atg/Liz-serpentinites and Atg-serpentinites ranges from 0.53 to 0.54. The occurrence of secondary olivine in Atg/Ol2-serpentinites is marked by a decrease of this ratio to 0.24–0.52.

The measured magnetite content of selected serpentinites and SSP is reported in Table 1. The magnetite mode progressively decreases with metamorphic grade (Fig. 6b). At the Montgenèvre ophiolite, the Liz-serpentinites have a mean magnetite mode of ∼6% whereas the mean magnetite mode of the Atg/Liz-serpentinite is about 3.3% (Table 1). At the Monte Maggiore, Atg/Liz-serpentinites display a mean magnetite mode varying from 2.2 to 4.9%, while Atg-serpentinites mean magnetite mode is about 1.3% (Table 1). At eclogite facies (Monviso and Lanzo massif), the mean magnetite mode is 3.4% for Atg/Liz-serpentinite and between 1 and 1.8% for Atg-serpentinite and Atg/Ol2-serpentinites (Table 1).

The selected SSP are plagioclase/spinel lherzolites. They display $Fe_2O_3{}^{Tot}{}_{(BR)}$ contents varying from 8.31 to 8.87 wt% and a $Fe^{3+}/Fe_{Total\,(BR)}$ ratio varying from 0.13 to 0.33 (Table 1). Their magnetite mode is less than 1%. According to Andreani et al. (2013), the $Fe^{3+}/Fe_{Total\,(BR)}$ ratio and magnetite mode of those rocks highly dependent on the local serpentinization degree of the rocks. Thus the observed variations in $Fe^{3+}/Fe_{Total\,(BR)}$ ratios and magnetite modes in these samples are most likely linked to
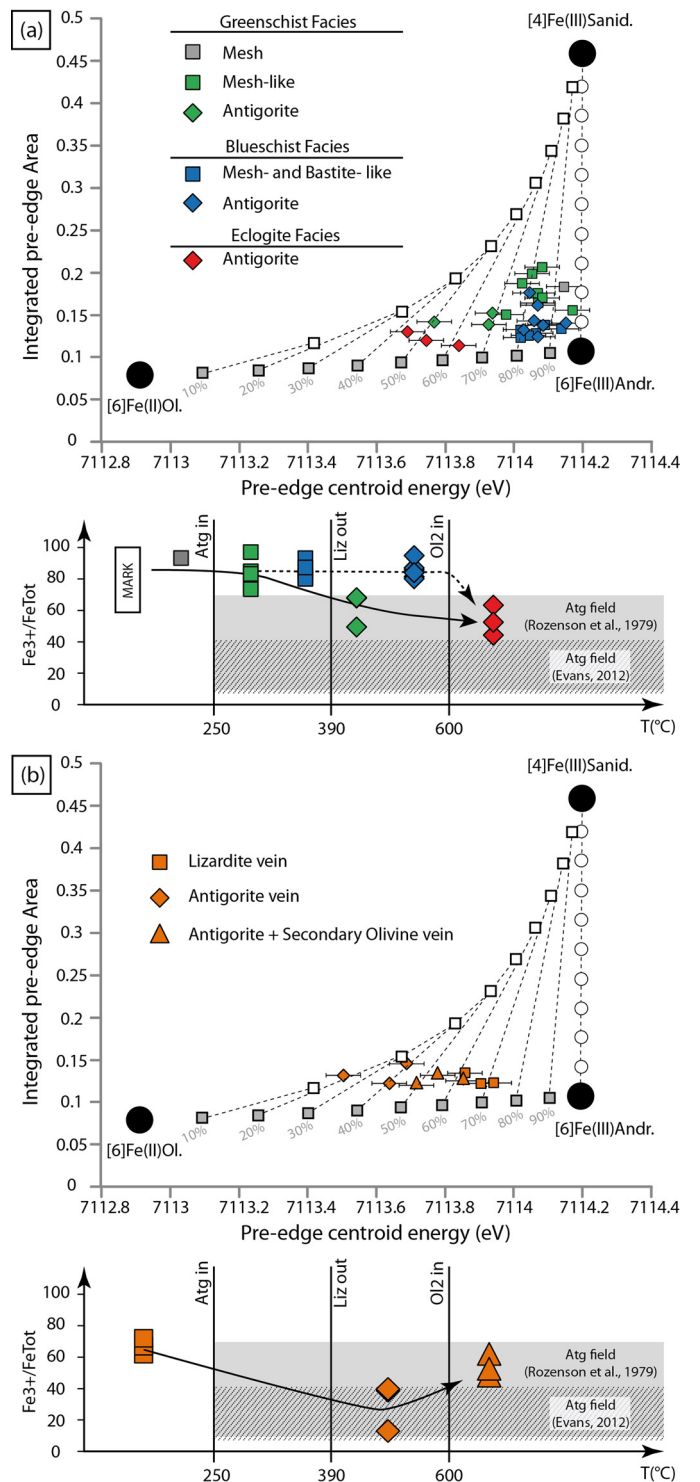

Fig. 5. Calibration grids modified after Wilke et al. (2001) and quantification of the Fe^{3+}/Fe_{Total} ratio in serpentine. The pre-edge centroid energy error is 0.05 eV (Wilke et al., 2001). (a) Evolution of serpentine pre-edge parameters (Integrated pre-edge Area Vs Pre-edge centroid energy) and corresponding evolution of the Fe^{3+}/Fe_{Total} ratio in serpentinites with prograde metamorphism. Two evolutions are displayed: the black arrow correspond to low Fe samples and the dashed arrow, to high Fe samples. MARK values are from Andreani et al. (2013). (b) Evolution of serpentine pre-edge parameters and corresponding evolution of the Fe^{3+}/Fe_{Total} ratio in serpentine veins from SSP. (See also Rozenson et al. (1979), Evans et al. (2012).)
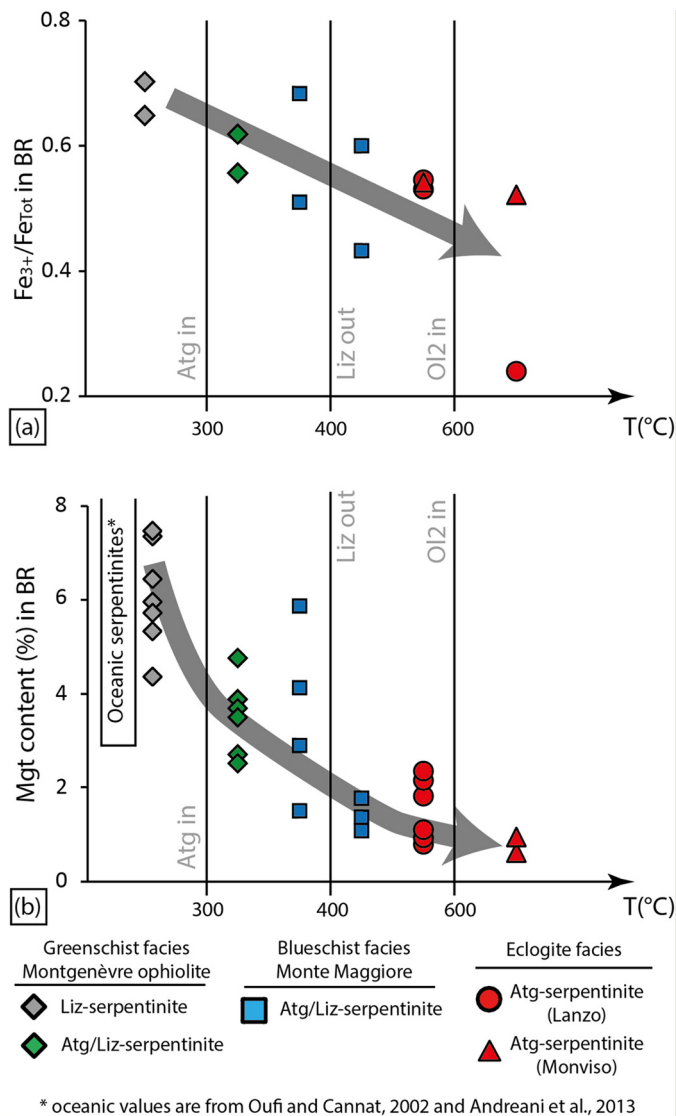
Fig. 6. Diagram presenting the evolution of (a) $Fe^{3+}/Fe_{Total\,(BR)}$ and (b) modal magnetite versus temperature. Sample temperature calibration is based on serpentine phase transitions drawn from thermodynamical data (Evans, 2004; and references therein), field observations (Schwartz et al., 2013) and experimental data (Bromiley and Pawley, 2003). The progressive increase of temperature is first marked by the growth of antigorite at 300 °C and then by the disappearance of lizardite at 400 °C (Evans, 2004; Schwartz et al., 2013) and finally by the occurrence of secondary olivine at 600 °C (Bromiley and Pawley, 2003).

the variable serpentinization degrees of the rocks, rather than the phase change of serpentine along prograde metamorphism.

4.2. In situ electron microprobe analysis

In situ measurements have been performed on 10 of the 13 serpentinites and on 5 of the 6 SSP samples. The microprobe analyses of serpentine minerals and secondary olivines are reported in Appendix A.

At the Montgenèvre ophiolite, the oceanic mesh and bastite textures of Liz-serpentinite display FeO contents of 2.4 to 3.5 wt%. In the Atg/Liz-serpentinites, the FeO contents of mesh- and bastite-like textures (Fig. 2c) range from 2.7 to 4.4 wt%, and the FeO contents of antigorite veins (Fig. 2c) vary from 3.6 to 4.4 wt%. In the Monte Maggiore ophiolite, samples MM8 and MM15 display heterogeneity in FeO: FeO contents vary respectively from 1.7 to 2.5 wt% and 2.8 to 4.4 wt%. In the Atg/Liz-serpentinites of Monviso ophiolite, the FeO content of mesh-like relicts ranges from 1.2 to

3 wt% and antigorite FeO contents vary from 0.8 to 3.5 wt%. In the Atg-serpentinites of Monviso and Lanzo ophiolites, the FeO content of antigorite (Fig. 3d) ranges from 3–5 wt%. In the same ophiolites, the FeO content of antigorite from Atg/Ol2-serpentinites (Fig. 3e) ranges from 1.8-4.8 wt%, while the composition of the secondary olivine is highly variable: in the Lanzo ophiolite, it varies from 12.4 to 15.4 wt% and in the Monviso ophiolite, the secondary olivine rims (FeO = 5.9–7.1 wt%) are depleted in FeO relative to the core (FeO = 10.6–11.4 wt%).

In the SSP, the FeO composition of serpentine veins is highly variable and depends on vein width or mineralogical site (olivine or pyroxene). The lizardite FeO content veins vary from 1.8 to 8.25 wt%. The FeO contents of antigorite veins ranges from 3.1 to 5.1 wt%. The secondary olivine FeO contents vary from 9.7 wt% to 11.5 wt%.

4.3. In situ XANES and pre-edge micro-analysis

The phase change from lizardite to antigorite is accompanied by a shift of the pre-edge peak centroid energy to lower values and a decrease of its integrated area (Fig. 4 and Fig. 5a) which corresponds to a decrease in serpentine Fe^{3+}/Fe_{Total} from 0.93 ± 0.06 at oceanic facies to 0.44 ± 0.06 at eclogite facies.

At the Montgenèvre ophiolite, in Atg/Liz-serpentinites (BCh6 and BCh9 samples), similar Fe^{3+}/Fe_{Total} ratios (0.97 ± 0.06 and 0.74 ± 0.06) are observed in mesh-like textures relative to oceanic textures of Liz-serpentinites from the same massif (ICh02, $Fe^{3+}/Fe_{Total} = 0.93 \pm 0.06$) and from modern mid-oceanic ridge ($Fe^{3+}/Fe_{Total} = 1$–0.6; Andreani et al., 2013). Antigorite veins in these samples have lower Fe^{3+}/Fe_{Total} ratios ranging from 0.69 ± 0.05 to 0.50 ± 0.06 relative to mesh textures. At the Monte Maggiore (MM8 sample), the mesh-like textures and antigorites display similar Fe^{3+}/Fe_{Total} ratios ranging respectively from 0.93 ± 0.06 to 0.80 ± 0.06 and from 0.95 ± 0.06 to 0.80 ± 0.06. These values are close to oceanic mesh textures. At eclogite facies (Monviso and Lanzo ophiolites), the antigorite Fe^{3+}/Fe_{Total} ratios vary from 0.63 ± 0.05 to 0.44 ± 0.06.

In the SSP, the lizardite veins display lower Fe^{3+}/Fe_{Total} ratios (0.72 ± 0.06 to 0.62 ± 0.05) relative to oceanic mesh textures from serpentinites (Fig. 5b). As observed previously, antigorite crystallization at the expense of lizardite is marked by a decrease in Fe^{3+}/Fe_{Total} (0.40 ± 0.05 to 0.13 ± 0.10). The crystallization of secondary olivine on prograde antigorite is marked by a new increase of Fe^{3+}/Fe_{Total} (0.62 ± 0.05 to 0.49 ± 0.05).

5. Discussion

5.1. The transition lizardite to antigorite in serpentinites

Numerous studies have shown that most of the major elements, in particular iron, are immobile during the serpentinization processes at the oceanic ridge (Andreani et al., 2013; Godard et al., 2008; Mével, 2003; Paulick et al., 2006) and during prograde metamorphism in subduction zones (Debret et al., 2013a, 2013b; Garrido et al., 2005; López Sánchez-Vizcaíno et al., 2005). In agreement with these previous results, no significant change of Fe content is observed in our serpentinites samples during prograde metamorphism (Table 1). This suggests that the fluid released from serpentinites during prograde metamorphism does not carry significant amount of Fe. Thus, a direct transfer of Fe from the slab to the mantle wedge cannot be considered as a mechanism for increasing the Fe^{3+}/Fe_{Total} of the mantle wedge peridotites and those of arc magmas. Nevertheless, modification of the Fe^{3+}/Fe_{Total} of the mantle wedge peridotites can result from the circulation of oxidized (H_2O, CO_2, SO_2, ...) or reduced (H_2, CH_4, H_2S, ...) fluids

and the production of such fluids will be a function of redox reactions occurring in the slab during prograde metamorphism, which should be reflected in the Fe^{3+}/Fe_{Total} of the prograde mineral assemblages.

Serpentinites from the studied ophiolites were formed close to the oceanic floor (Angiboust et al., 2011; Caby, 1995; Debret et al., 2013a). In such context, serpentinites are expected to be formed in a fluid dominated system and to have high magnetite and Fe^{3+} contents (Andreani et al., 2013; Frost et al., 2013; Oufi et al., 2002). The Montegenèvre ophiolite preserves poorly metamorphosed Liz-serpentinites which have similar magnetite content and $Fe^{3+}/Fe_{Total\,(BR)}$ ratio relative to oceanic serpentinites from modern settings (Fig. 6). Furthermore, in this ophiolite the mesh and mesh-like textures display similar Fe^{3+}/Fe_{Total} ratio to oceanic serpentine from modern settings (Fig. 5). This suggests that the studied serpentinites started with high Fe^{3+}/Fe_{Total} ratios prior to subduction that were close to those displayed by modern abyssal serpentinites.

During the first stage of subduction, from greenschist to eclogite facies, the transition from lizardite to antigorite is first marked by the formation of Atg/Liz-serpentinite and then of Atg-serpentinite. During this phase transition, the $Fe^{3+}/Fe_{Total(BR)}$ ratio decreases from 0.65–0.7 in Liz-serpentinites to 0.53–0.54 in Atg-serpentinites (Fig. 6a). The selected samples correspond to peridotites that have been largely serpentinized during the oceanic stage (distal continental margin or mid-ocean ridge environment; Debret et al., 2013a, 2013b; Hattori and Guillot, 2007; Lafay et al., 2013; Schwartz et al., 2013) and then evolved without any interaction with external fluids during subduction (Debret et al., 2013b), in contrast to serpentinites from the Queyras accretionary prism, which evolved in close proximity to metasediments (Schwartz et al., 2013) and experienced substantial fluid contamination as evidenced from As, Sb or Cs enrichments in antigorite (Lafay et al., 2013). Hence the variations in $Fe^{3+}/Fe_{Total(BR)}$ observed in our samples are unlikely to reflect either contamination processes operating during subduction or variable serpentinization degrees of the initial oceanic peridotite. However, these results show that the reaction lizardite to antigorite is a redox reaction accompanied by a reduction of about 25% of the $Fe_2O_3^{Tot}{}_{(BR)}$ (Fig. 6a). Among the minerals involved during this phase transition, magnetite and serpentine minerals are the main iron carriers and they are both affected by reduction processes. Indeed, during subduction, the growth of antigorite at the expense of lizardite is associated with a decrease of modal magnetite (Fig. 6b) due to a progressive dissolution of the magnetite grains at mesh rims (Fig. 2c). This decrease is more rapid in Cpx- and Sp-poor samples (i.e. Fe-poor samples), than in Cpx- and Sp-rich samples (i.e. Fe-rich samples, Table 1) because Cpx and Sp are respectively transformed into Mgt2 + Atg and Mgt2 + Cr-Sp + Atg assemblages (Fig. 3a–d). Nevertheless, in pure Atg-serpentinites, irrespective of the primary mineral mode, the oceanic lizardite, mantle clinopyroxene or spinel are absent, and the magnetite modal abundance drops down to 1%. Hence, magnetite has been progressively consumed and may even act as a reactant during the prograde redox reaction lizardite to antigorite. This observation also suggests that magnetite is metastable in Atg-serpentinite at eclogite facies.

The decrease in modal magnetite content is inversely correlated to the Fe content of serpentine (Fig. 7), which reflects the fact that the Fe lost during magnetite dissolution is transferred to serpentine. Thus, there is no room for Fe addition by fluids to the rock during the transition from lizardite to antigorite in our samples (Frost, 1991; O'Hanley and Dyar, 1993). This is in good agreement with our previous geochemical study attesting that the alpine ophiolites have evolved in relative closed system during subduction (Debret et al., 2013b). It also confirms the immobile character of Fe during serpentinization at the metric scale.
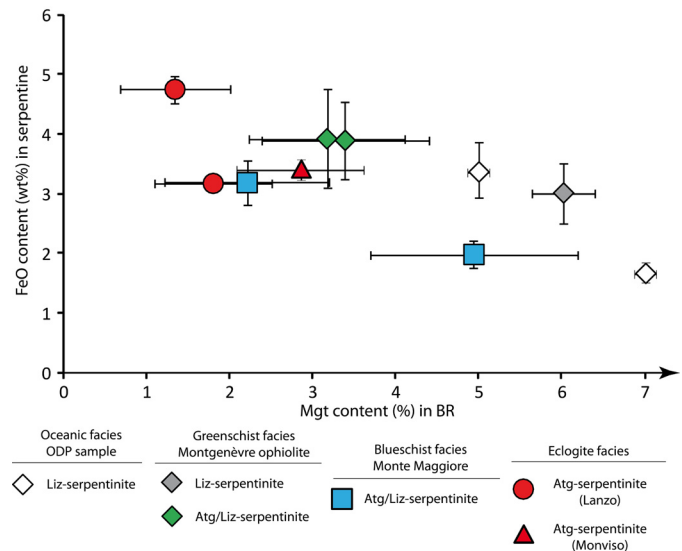

Fig. 7. Diagram of the mean values of FeO content in serpentine versus modal magnetite in bulk rock (BR). The error bars correspond to the standard deviation of the mean values. The data indicate these parameters are inversely correlated.

Fig. 5a shows that Fe^{3+}/Fe_{Total} ratio in serpentine minerals decreases non-linearly with prograde metamorphism and this tendency varies with $Fe_2O_3^{Tot}{}_{(BR)}$ content of the rock during first reaction stages. At the Montgenèvre ophiolite, in Fe-low Atg/Liz-serpentinites, the Fe^{3+}/Fe_{Total} ratio decreases from 0.74–0.97 in the mesh-like texture to 0.50–0.69 in the antigorite. However, at the Monte Maggiore locality, in Fe-rich Atg/Liz-serpentinites, this ratio is constant during the recrystallization of mesh-like texture (0.80–0.93) into antigorite (0.80–0.95), and remains close to oceanic serpentines. At eclogite facies, in Atg- and Atg/Ol2-serpentinites, the antigorite Fe^{3+}/Fe_{Total} (0.44–0.63) is lower irrespective of the $Fe_2O_3^{Tot}{}_{(BR)}$ content of the bulk rock (Table 1). Thus, the redox reaction associated with the whole lizardite → antigorite transition finally represents a reduction of ∼50% of the serpentine Fe.

The reduction of Fe in the bulk rock is the result of a decrease of the amount of magnetite and a reduction of the Fe in serpentine. However, this decrease does not constitute the full redox reaction taking place during the lizardite/antigorite transition. Indeed, considering a decrease of $Fe^{3+}/Fe_{Total\,(BR)}$ ratio from 0.7 to 0.5 during the lizardite/antigorite transition (Table 1), the iron reduction can be expressed as:

$$0.35Fe_2O_3 + 0.3FeO \rightarrow 0.25Fe_2O_3 + 0.5FeO + 0.05O_{2(aq)} \qquad (1)$$
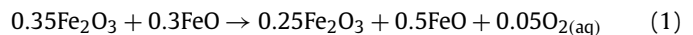
According to this reaction, the reduction of iron liberates oxygen that could oxidize reduced oceanic species.

In intra-oceanic serpentinites, sulfides occur as disseminated micrometric grains in mesh or bastite textures (Alt and Shanks, 2003; Delacour et al., 2008a). During subduction, S is removed from serpentinites during the prograde transition lizardite to antigorite suggesting that sulfides are dissolved and then released in a fluid phase (Debret et al., 2014). Considering the reduction of iron expressed in Eq. (1), a more complete reaction involving the oxidation of sulfides could be written as:

$$0.35Fe_2O_3 + 0.3FeO + 0.025S^{2-}$$
$$\rightarrow 0.25Fe_2O_3 + 0.5FeO + 0.025SO_4^{2-}{}_{(aq)} \qquad (2)$$
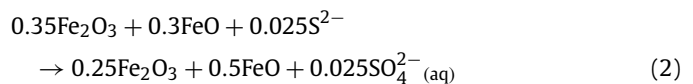
Based on the iron content of serpentinites, Eq. (2) should lead to a decrease of about 4000 ppm in sulfide concentration in the bulk rock during the lizardite to antigorite transition. Such a mobilization is higher than the sulfur decrease of about 500 ppm measured

by Debret et al. (2014). Potentially, other reduced species may also be oxidized which would offset this effect, such as reduced oceanic carbon (Delacour et al., 2008b; Pasini et al., 2013), residual CH_4 or H_2 (e.g. Evans et al., 2012, 2013), and/or the release of oxygen as mentioned in Eq. (1). Furthermore, reaction (1) and (2) are a subset of a continuum of reactions occurring into the slab and other fluid/rock interactions need to be considered in order to better constrain the entire redox budget of the slab.

5.2. The antigorite dehydration into secondary olivine.

In alpine serpentinites, few variations of serpentine Fe redox state have been observed with antigorite breakdown (Tables 1 and 2). The secondary olivine assemblages represent less than ~10% of the rock. Their formation is not sufficient to modify the redox state of the remaining antigorite. On the other hand, in the SSP, the serpentine veins correspond to relatively closed systems where the local dehydration degree can reach ~40%.

In the SSP, the oceanic lizardite veins display lower Fe^{3+}/Fe_{Total} ratio than the ones observed in Liz-serpentinites. This is inherited from the lower serpentinization degree of the SSP on the seafloor since experimental and natural results have shown that the magnetite mode and Fe^{3+}/Fe_{Total} ratio of the serpentine progressively increase with the serpentinization degree (Andreani et al., 2013; Marcaillou et al., 2011).

In SSP, antigorite veins have a lower Fe^{3+}/Fe_{Total} ratio than lizardite veins. This corresponds to a reduction of about 50% of the Fe contained in serpentine. The occurrence of secondary olivine is accompanied with a new increase of the Fe^{3+}/Fe_{Total} ratio in antigorite that increases from 0.1–0.4 in prograde antigorite to 0.5–0.6 (Fig. 5b) in the remaining antigorite associated with secondary olivine.

Previous studies realized on the meta-peridotites of Almirez massif have proposed that antigorite dehydration results in the growth of enstatite, olivine and chlorite and the release of H_2O (Trommsdorff et al., 1998). The prograde antigorite breakdown occurs through a series of continuous reactions forming antigorite associated with olivine and chlorite (Chollet et al., 2011; Padrón-Narvarta et al., 2008, 2011, 2013). Even if enstatite and olivine mainly incorporate Fe^{2+}, the full redox equilibria of dehydration reactions are poorly constrained because the changes in Fe oxidation state of antigorite and chlorite as well as the mode of magnetite remain unknown. In alpine ophiolites, only the first stage of serpentinite dehydration has been observed in the Monviso and Lanzo ophiolites. This episode is accompanied by the quasi-total disappearance of magnetite (Fig. 6b) and by the formation of a Fe^{3+} bearing-antigorite and secondary olivine assemblage (Debret et al., 2013a; Schwartz et al., 2013). Our XANES measurements indicate a redistribution of Fe during the first stages of antigorite breakdown. Indeed, the solubility of Fe^{3+} in olivine is extremely low, and thus it is preferentially partitioned into antigorite during the dehydration reaction. The incorporation of Fe^{3+}, as well as Al^{3+}, into the antigorite structure could stabilize it to higher temperature and pressure (Bromiley and Pawley, 2003; Eggler and Ehmann, 2010; Padrón-Narvarta et al. 2008, 2011, 2013) allowing its crystallization in equilibrium with secondary olivine.

6. Conclusions

During subduction, with the increase of P–T conditions from greenschist to blueschist facies, the oceanic lizardite and chrysotile assemblages are progressively recrystallized into antigorite. This episode is accompanied by a decrease of $Fe^{3+}/Fe_{Total(BR)}$ without changes of $Fe_2O_3^{Tot}{}_{(BR)}$ attesting for a reduction of Fe in the serpentinite. Among the minerals involved during this phase change, magnetite and serpentine are the main iron carriers and

they are both affected by these reduction processes. Magnetite is progressively dissolved during lizardite destabilization, and in Atg-serpentinites, the antigorite has a lower Fe^{3+}/Fe_{Total} than its precursor. The reduction of iron in the bulk rock is accompanied by the release of oxygen, which therefore potentially drives to the oxidation and mobilization of reduced phases such as sulfide or carbon into a fluid phase (e.g. H_2O, SO_X or CO_2). These fluids could have a great oxidizing potential, e.g., during mantle wedge metasomatism by SO_2 fluids, 1 mole of S (S^{2+}) can oxidize 6 moles of Fe^{2+} during the SO_2 reduction to sulfide (S^{2-}). It also suggests that the redox change during the transition lizardite to antigorite controls the formation of a fluid phase and thus the mobility of volatile and/or trace elements.

At greater depth, the nature of the released fluids remains unclear. The first stage of antigorite breakdown is accompanied by a redistribution of iron forming a Fe^{3+}-rich antigorite associated with Fe^{2+}-olivine while previous studies (e.g. Padrón-Narvarta et al., 2011) have shown that during the full dehydration of the serpentinite, the antigorite is replaced by enstatite, olivine and chlorite assemblages. Even if the redox state of Fe in chlorite and the magnetite mode evolution remain unknown, it seems that this episode is accompanied by a reduction of Fe and a massive release of H_2O (Padrón-Narvarta et al., 2011).

Appendix A. Supplementary material

Supplementary materials (MMC 1 and MMC 2) related to this article can be found online at http://dx.doi.org/10.1016/j.epsl.2014.05.038.

References

Alt, J., Shanks, W.C.S., 2003. Serpentinization of abyssal peridotites from the MARK area, Mid-Atlantic Ridge: sulfur geochemistry and reaction modeling. Geochim. Cosmochim. Acta 67, 641–653.

Andersen, T., Neumann, E.R., 2001. Fluid inclusions in mantle xenoliths. Lithos 55, 301–320.

Andreani, M., Mével, C., Boullier, A.-M., Escartin, J., 2007. Dynamic control on serpentine crystallization in veins: constraints on hydration processes in oceanic peridotites. Geochem. Geophys. Geosyst. 8, Q02012. http://dx.doi.org/10.1029/2006GC001373.

Andreani, M., Muñoz, M., Marcaillou, C., Delacour, A., 2013. μXANES study of iron redox state in serpentine during oceanic serpentinization. Lithos 178, 70–83.

Angiboust, S., Langdon, R., Agard, P., Waters, D., Chopin, C., 2011. Eclogitization of the Monviso ophiolite (W. Alps) and implications on subduction dynamics. J. Metamorph. Geol. 30, 37–61.

Arculus, R.J., 1994. Aspects of magma genesis in arcs. Lithos 33, 189–208.

Bach, W., Paulick, H., Garrido, C.J., Ildefonse, B., Meurer, W.P., Humphris, S., 2006. Unravelling the sequence of serpentinization reactions: petrography, mineral chemistry, and petrophysics of serpentinites from MAR 15°N (ODP leg 209, site 1274). Geophys. Res. Lett. 33, L13306.

Berndt, M.E., Allen, D.E., Seyfried, W.E., 1996. Reduction of CO_2 during serpentinization of olivine at 300 °C and 500 bar. Geology 24, 351–354.

Berry, A.J., O'Neill, H.S.C., Jayasuriya, K., Campbell, S., Foran, G., 2003. XANES calibrations for the oxidation state of iron in a silicate glass. Am. Mineral. 88, 967–977.

Berry, A.J., Yaxley, G.M., Woodland, A.B., Foran, G.J., 2010. A XANES calibration for determining the oxidation state of iron in mantle garnet. Chem. Geol. 278, 31–37.

Bolfan-Casanova, B., Muñoz, M., McCammon, C., Deloule, E., Férot, A., Demouchy, S., France, L., Andrault, D., Pascarelli, S., 2012. Ferric iron and water incorporation in wadsleyite under hydrous and oxidizing conditions: a XANES, Mössbauer, and SIMS study. Am. Mineral. 97, 1483–1493.

Bromiley, G.D., Pawley, A.R., 2003. The stability of antigorite in the systems $MgO–SiO_2–H_2O$ (MSH) and $MgO–Al_2O_3–SiO_2–H_2O$ (MASH): the effects of Al^{3+} substitution on high-pressure stability. Am. Mineral. 88, 99–108.

Caby, R., 1995. Plastic deformations of gabbros in a slow-spreading mesozoic Ridges: example of the Montgenèvre Ophiolite, Western Alps. In: Vissers, R.L.M., Nicolas, A. (Eds.), Proc. Workshop on Mantle and Lower Crust Exposed in Oceanic Ridges and in Ophiolites. Kluwer, Dordrecht, pp. 123–145.

Canales, J.P., Collins, J.A., Escartin, J., Detrick, R.S., 2000. Seismic structure across the rift valley of the Mid-Atlantic ridge at 23°20′N (MARK area): implications for crustal accretion processes at slow-spreading ridges. J. Geophys. Res. 105, 28411–28425.

Cannat, M., Mével, C., Maïa, M., Deplus, C., Durand, C., Gente, P., Agrinier, P., Belarouchi, A., Dubuisson, G., Humler, E., Reynolds, J., 1995. Thin crust, ultramafic exposure and rugged faulting patterns at the Mid-Atlantic Ridge (22°24′N). Geology 23, 49–52.

Cannat, M., Fontaine, F., Escartín, 2010. Serpentinization and associated hydrogen and methane fluxes at slow spreading ridges. In: Geophysical Monograph Series, vol. 188. American Geophysical Union, pp. 241–263.

Chalot-Prat, F., 2005. An undeformed ophiolite in the Alps: field and geochemical evidence for a link between volcanism and shallow plate tectonic processes. In: Foulger, G.R., Natland, J.H., Presnall, D.C., Anderson, D.L. (Eds.), Plate, Plumes, and Paradigms. In: Special Papers, vol. 388. Geological Society of America, pp. 751–780.

Charlou, J., Donval, J.P., Fouquet, Y., Jean-Baptiste, P., Holm, N., 2002. Geochemistry of high H_2 and CH_4 vent fluids issuing from ultramafic rocks at the Rainbow hydrothermal field (36°14′N, MAR). Chem. Geol. 191, 345–359.

Chollet, M., Daniel, I., Koga, K.T., Morard, G., van de Moortèle, B., 2011. Kinetics and mechanism of antigorite dehydration: implications for subduction zone seismicity. J. Geophys. Res. 116, B04203.

Debret, B., Nicollet, C., Andreani, M., Schwartz, S., Godard, M., 2013a. Three steps of serpentinization in an eclogitized oceanic serpentinization front (Lanzo Massif – Western Alps). J. Metamorph. Geol. 31, 165–186.

Debret, B., Andreani, M., Godard, M., Nicollet, C., Schwartz, S., 2013b. Trace element behavior during serpentinization/deserpentinization of an eclogitized oceanic lithosphere: a LA-ICPMS study of the Lanzo ultramafic massif (Western Alps). Chem. Geol. 357, 117–133.

Debret, B., Koga, K., Nicollet, C., Andreani, M., Schwartz, S., 2014. F, Cl and S input via serpentinite in subduction zones: implications on the nature of the fluid released at depth. Terra Nova 26, 96–101.

Delacour, A., Früh-Green, G.L., Bernasconi, S.M., 2008a. Sulfur mineralogy and geochemistry of serpentinites and gabbros of the Atlantis Massif (IODP Site U1309). Geochim. Cosmochim. Acta 72, 5111–5127.

Delacour, A., Früh-Green, G.L., Bernasconi, S.M., Schaeffer, P., Kelley, D.S., 2008b. Carbon geochemistry of serpentinites in the Lost City hydrothermal system. Geochim. Cosmochim. Acta 72, 3681–3702.

Eggler, D.H., Ehmann, A.N., 2010. Rate of antigorite dehydration at 2 GPa applied to subduction zones. Am. Mineral. 95, 761–769.

Evans, B.W., 2004. The serpentinite multisystem revisited: chrysotile is metastable. Int. Geol. Rev. 46, 479–506.

Evans, K.A., Tomkins, A., 2011. The relationship between subduction zone redox budget and arc magma fertility. Earth Planet. Sci. Lett. 308, 401–409.

Evans, B.W., Dyar, M.D., Kuehner, S.M., 2012. Implications of ferrous and ferric iron in antigorite. Am. Mineral. 97, 184–196.

Evans, B.W., Hattori, K., Baronnet, A., 2013. Serpentinite: what, why, where? Elements 9, 99–106.

Evans, K.A., Dyar, D.M., Reddy, S.M., Lanzirotti, A., Adams, D.T., Tailby, N., 2014. Variation in XANES in biotite as a function of orientation, crystal composition and metamorphic history. Am. Mineral. 99, 443–457.

Farges, F., Brown Jr., G., Petit, P., Muñoz, M., 2001. Transition elements in water-bearing silicate glasses/melts. Part I. A high-resolution and anharmonic analysis of Ni coordination environments in crystals, glasses, and melts. Geochim. Cosmochim. Acta 65, 1665–1678.

Frost, B.R., 1991. Magnetic petrology and factors that control the occurrence of magnetite in crustal rocks. Mineral. Soc. Am. Rev. Mineral. 25, 489–509.

Frost, D.J., McCammon, C., 2008. The redox state of Earth's mantle. Annu. Rev. Earth Planet. Sci. 36, 389–420.

Frost, B.R., Evans, K.A., Swapp, S.M., Beard, J.S., Mothersole, F.E., 2013. The process of serpentinization in dunite from New Caledonia. Lithos 178, 24–39.

Fuchs, Y., Linares, J., Mellini, M., 1998. Mössbauer and infrared spectrometry of lizardite-1T from Monte Fico, Elba. Phys. Chem. Miner. 26, 111–115.

Fumagalli, P., Poli, S., 2005. Modelling metamorphic rocks in complex systems: present-day developments in high pressure experimental petrology. Period. Mineral. 73, 197–208.

Garrido, C.J., López Sánchez-Vizcaíno, V., Gómez-Pugnaire, M.T., Trommsdorff, V., Alard, O., Bodinier, J.L., Godard, M., 2005. Enrichment of HFSE in chlorite-harzburgite produced by high-pressure dehydration of antigorite–serpentinite: implications for subduction magmatism. Geochem. Geophys. Geosyst. 6, Q01J15. http://dx.doi.org/10.1029/2004GC000791.

Godard, M., Lagabrielle, Y., Alard, O., Harvey, J., 2008. Geochemistry of the highly depleted peridotites drilled at ODP Sites 1272 and 1274 (Fifteen-Twenty Fracture Zone, Mid-Atlantic Ridge): implications for mantle dynamics beneath a slow spreading ridge. Earth Planet. Sci. Lett. 267, 410–425.

Hattori, K.H., Guillot, S., 2007. Geochemical character of serpentinites associated with high- to ultrahigh-pressure metamorphic rocks in the Alps, Cuba, and the Himalayas: recycling of elements in subduction zones. Geochem. Geophys. Geosyst. 8, Q09010. http://dx.doi.org/10.1029/2007GC001594.

Jackson, M.D., Ohnenstetter, M., 1981. Peridotite and gabbroic structures in the Monte Maggiore massif, Alpine Corsica. J. Geol. 89, 703–719.

Kelley, K., Cottrell, E., 2009. Water and the oxidation state of subduction zone magmas. Science 325, 605–607.

Klein, F., Bach, W., 2009. Fe–Ni–Co–O–S phase relations in peridotite seawater interactions. J. Petrol. 50, 37–59.

Klein, F., Bach, W., Jöns, N., McCollom, T., Moskowitz, B., Berquo, T., 2009. Iron partitioning and hydrogen generation during serpentinization of abyssal peridotites from 15°N on the Mid-Atlantic Ridge. Geochim. Cosmochim. Acta 73, 6868–6893.

Klein, F., Bach, W., McCollom, T.M., 2013. Compositional controls on hydrogen generation during serpentinization of ultramafic rocks. Lithos 178, 55–69.

Lafay, R., Deschamps, F., Schwartz, S., Guillot, S., Godard, M., Debret, B., Nicollet, C., 2013. High-pressure serpentinites, a trap-and-release system controlled by metamorphic conditions: example from the Piedmont zone of the western Alps. Chem. Geol. 343, 38–54.

Lagabrielle, Y., Cannat, M., 1990. Alpine Jurassic ophiolites resemble the modern central Atlantic basement. Geology 18, 319–322.

Lagabrielle, Y., Fudural, S., Kienast, J.R., 1989. La couverture océanique des ultrabasites de Lanzo (Alpes occidentales): arguments lithostratigraphiques et pétrologiques. Geodin. Acta 3, 43–55.

Lee, C.T.A., Luffi, P., Le Roux, V., Dasgupta, R., Albarede, F., Leeman, W., 2010. The redox of arc mantle using Zn/Fe systematics. Nature 468, 681–685.

Li, X.P., Rahn, M., Bucher, K., 2004. Serpentinites of the Zermatt–Saas ophiolite complex and their texture evolution. J. Metamorph. Geol. 22, 159–177.

Lombardo, B., Rubatto, D., Castelli, D., 2002. Ion microprobe U–Pb dating of zircon from a Monviso metaplagiogranite: implications for the evolution of the Piedmont-Liguri Tethys in the western Alps. Ofioliti 27, 109–117.

López Sánchez-Vizcaíno, V., Trommsdorff, V., Gómez-Pugnaire, M.T., Garrido, C.J., Müntener, O., Connolly, J.A.D., 2005. Petrology of titanian clinohumite and olivine at the high-pressure breakdown of antigorite serpentinite to chlorite harzburgite (Almirez Massif, S. Spain). Contrib. Mineral. Petrol. 149, 627–646.

Malvoisin, B., Chopin, C., Brunet, F., Galvez, M.E., 2011. Low-temperature wollastonite formed by carbonate reduction: a marker of serpentinite redox conditions. J. Petrol. 53, 159–176.

Malvoisin, B., Carlut, J., Brunet, F., 2012. Serpentinization of oceanic peridotites: 1. A high-sensitivity method to monitor magnetite production in hydrothermal experiments. J. Geophys. Res. 117, B01104.

Manatschal, G., Sauter, D., Karpoff, A.M., Masini, E., Mohn, G., Lagabrielle, Y., 2011. The Chenaillet Ophiolite in the French/Italian Alps: an ancient analogue for an Oceanic Core Complex? Lithos 124, 169–184.

Marcaillou, C., Muñoz, M., Vidal, O., Parra, T., Harfouche, M., 2011. Mineralogical evidence for H_2 degassing during serpentinization at 300 °C/300 bar. Earth Planet. Sci. Lett. 303, 281–290.

McCollom, T.M., Bach, W., 2009. Thermodynamic constraints on hydrogen generation during serpentinization of ultramafic rocks. Geochim. Cosmochim. Acta 73, 856–875.

Mével, C., 2003. Serpentinization of abyssal peridotites at mid-ocean ridges. C. R. Géosci. 335, 825–852.

Mével, C., Caby, R., Kienast, J.R., 1978. Amphibolite facies conditions in oceanic crust: example of amphibolitized flaser gabbros and amphibolites from the Chenaillet ophiolite massif (Hautes Alpes, France). Earth Planet. Sci. Lett. 39, 98–108.

Muñoz, M., Vidal, O., Marcaillou, C., Sakura, P., Mathon, O., Farges, F., 2013. Iron oxidation state in phyllosilicate single crystals using Fe–K edge and XANES spectroscopy: Effects of the linear polarization of the synchrotron X-ray beam. Am. Mineral. 98, 1187–1197.

Müntener, O., Hermann, J., Trommsdorff, V., 2000. Cooling history and exhumation of lower-crustal granulite and upper mantle (Malenco, Eastern Central Alps). J. Petrol. 41, 175–200.

Nicollet, C., Chazot, G., Cloquet, C., 2001. Evolution géodynamique d'une portion de manteau: Pétrologie et Trajet $P–T–t$ des Lherzolites et Gabbros associés du Monte Maggiore, Cap Corse. Journées de la Société Géologique de France, Clermont Fd.

O'Hanley, D.S., Dyar, M.D., 1993. The composition of lizardite 1 T and the formation of magnetite in serpentinites. Am. Mineral. 78, 391–404.

O'Reilly, W., 1984. Rock and Mineral Magnetism. Blackie, London. 220 pp.

Oufi, O., Cannat, M., Horen, H., 2002. Magnetic properties of variably serpentinized abyssal peridotites. J. Geophys. Res. 107, 1978–2012.

Padrón-Navarta, J.A., López Sánchez-Vizcaíno, V., Garrido, C.J., Gómez-Pugnaire, M.T., Jabaloy, A., Capitani, G., Mellini, M., 2008. Highly ordered antigorite from Cerro del Almirez HP–HT serpentinites, SE Spain. Contrib. Mineral. Petrol. 156, 679–688.

Padrón-Navarta, J.A., López Sánchez-Vizcaíno, V., Garrido, C.J., Gomez-Pugnaire, M.T., 2011. Metamorphic record of high-pressure dehydration of antigorite serpentinite to chlorite harzburgite in a subduction setting (Cerro del Almirez, Nevado-Filabride Complex, Southern Spain). J. Petrol. 52, 2047–2078.

Padrón-Navarta, J.A., López Sánchez-Vizcaíno, V., Hermann, J., Connolly, J.A.D., Garrido, C.J., Gómez-Pugnaire, M.T., Marchesi, C., 2013. Tschermak's substitution in antigorite and consequences for phase relations and water liberation in high-grade serpentinites. Lithos 178, 186–196.

Parkinson, I.J., Arculus, R.J., 1999. The redox state of subduction zones: insights from arc-peridotites. Chem. Geol. 160, 409–423.

Pasini, V., Brunelli, D., Dumas, P., Sandt, C., Frederick, J., Benzerara, K., Bernard, S., Ménez, B., 2013. Low temperature hydrothermal oil and associated biological precursors in serpentinites from Mid-Ocean Ridge. Lithos 178, 84–95.

Paulick, H., Bach, W., Godard, M., De Hoog, J.C.M., Suhr, G., Harvey, J., 2006. Geochemistry of abyssal peridotites (Mid-Atlantic Ridge, 15°20′N, ODP Leg 209): implications for fluid/rock interaction in slow spreading environments. Chem. Geol. 234, 179–210.

Pelletier, L., Müntener, O., 2006. High-pressure metamorphism of the Lanzo peridotite and its oceanic cover, and some consequences for the Sezia–Lanzo zone (northwestern Italian Alps). Lithos 90, 111–130.

Piccardo, G.B., Guarnieri, L., 2010. The Monte Maggiore peridotite (Corsica, France): a case study of mantle evolution in the Ligurian Tethys. Special Publications, vol. 337. Geological Society, London, pp. 7–45.

Ravel, B., Newville, M., 2005. ATHENA, ARTEMIS, HEPHAESTUS: data analysis for X-ray absorption spectroscopy using IFEFFIT. J. Synchrotron Radiat. 12, 537–541.

Reynard, B., 2013. Serpentine in active subduction zones. Lithos 178, 171–185.

Reynard, B., Nakajima, J., Kawakatsu, H., 2010. Earthquakes and plastic deformation of anhydrous slab mantle in double Wadati–Benioff zones. Geophys. Res. Lett. 37, 24.

Rozenson, I., Bauminger, E.R., Heller-Kallai, L., 1979. Mössbauer spectra of 1:1 phyllosilicates. Am. Mineral. 64, 893–901.

Savov, I.P., Ryan, J.G., D'Antonio, M., Kelley, K., Mattie, P., 2005. Geochemistry of serpentinized peridotites from the Mariana Forearc–Conical Seamount, ODP Leg 125: implications for the elemental recycling at subduction zones. Geochem. Geophys. Geosyst. 6, Q04J15. http://dx.doi.org/10.1029/2004GC000777.

Savov, I.P., Ryan, J.G., D'Antonio, M., Fryer, P., 2007. Shallow slab fluid release across and along the Mariana arc-basin system: insights from geochemistry of serpentinized peridotites from the Mariana fore arc. J. Geophys. Res. 112, B09205.

Scambelluri, M., Tonarini, S., 2012. Boron isotope evidence for shallow fluid transfer across subduction zones by serpentinized mantle. Geology 40, 907–910.

Schwartz, S., Allemand, P., Guillot, S., 2001. Numerical model of the effect of serpentinites on the exhumation of eclogitic rocks: insights from the Monviso ophiolitic massif (Western Alps). Tectonophysics 342, 193–206.

Schwartz, S., Guillot, S., Reynard, B., Lafay, R., Debret, B., Nicollet, C., Lanari, P., Auzende, A.L., 2013. Pressure–temperature estimates of the lizardite/antigorite transition in high pressure serpentinites. Lithos 178, 197–210.

Seyfried, W.E., Foustoukos, D.I., Fu, Q., 2007. Redox evolution and mass transfer during serpentinization: an experimental and theoretical study at 200°C, 500 bar with implications for ultramafic-hosted hydrothermal systems at mid-ocean ridges. Geochim. Cosmochim. Acta 71, 3872–3886.

Song, S., Su, L., Niu, Y., Lai, Y., Zhang, L., 2009. CH_4 inclusions in orogenic harzburgite: evidence for reduced slab fluids and implication for redox melting in mantle wedge. Geochim. Cosmochim. Acta 73, 1737–1754.

Stolper, E.M., Newman, S., 1994. The role of water in the petrogenesis of Mariana trough magmas. Earth Planet. Sci. Lett. 121, 293–325.

Trommsdorff, V., López Sánchez-Vizcaíno, V., Gomez-Pugnaire, M.T., Müntener, O., 1998. High pressure breakdown of antigorite to spinifex-textured olivine and orthopyroxene, SE Spain. Contrib. Mineral. Petrol. 132, 139–148.

Ulmer, P., Trommsdorff, V., 1995. Serpentine stability to mantle depths and subduction-related magmatism. Science 268, 858–861.

Vils, F., Müntener, O., Kalt, A., Ludwig, T., 2011. Implications of the serpentine phase transition on the behaviour of beryllium and lithium–boron of subducted ultramafic rocks. Geochim. Cosmochim. Acta 75, 1249–1271.

Vitale Brovarone, A., Beyssac, O., Malavieille, J., Molli, G., Beltrando, M., Compagnoni, R., 2013. Stacking and metamorphism of continuous segments of subducted lithosphere in a high-pressure wedge: the example of Alpine Corsica (France). Earth-Sci. Rev. 116, 35–56.

Wilke, M., Farges, F., Petit, P.E., Gordon, E.B., Martin, F., 2001. Oxidation state and coordination of Fe in minerals: an Fe K-XANES spectroscopic study. Am. Mineral. 86, 714–730.

Wunder, B., Schreyer, W., 1997. Antigorite: high-pressure stability in the system. Lithos 41, 213–227.

Wunder, B., Wirth, R., Gottschalk, M., 2001. Antigorite: Pressure and temperature dependence of polysomatism and water content. Eur. J. Mineral. 13, 485–495.